Check for updates



NANO · MICRO small
www.small-journal.com

# Machine Learning-Based and Experimentally Validated Optimal Adhesive Fibril Designs

*Donghoon Son, Ville Liimatainen, and Metin Sitti**

**Setae, fibrils located on a gecko's feet, have been an inspiration of synthetic dry microfibrillar adhesives in the last two decades for a wide range of applications due to unique properties: residue-free, repeatable, tunable, controllable and silent adhesion; self-cleaning; and breathability. However, designing dry fibrillar adhesives is limited by a template-based-design-approach using a pre-determined bioinspired T- or wedge-shaped mushroom tip. Here, a machine learning-based computational approach to optimize designs of adhesive fibrils is shown, exploring a much broader design space. A combination of Bayesian optimization and finite element methods creates novel optimal designs of adhesive fibrils, which are fabricated by two-photon-polymerization-based 3D microprinting and double-molding-based replication out of polydimethylsiloxane. Such optimal elastomeric fibril designs outperform previously proposed designs by maximum 77% in the experiments of dry adhesion performance on smooth surfaces. Furthermore, finite-element-analyses reveal that the adhesion of the fibrils is sensitive to the 3D fibril stem shape, tensile deformation, and fibril microfabrication limits, which contrast with the previous assumptions that mostly neglect the deformation of the fibril tip and stem, and focus only on the fibril tip geometry. The proposed computational fibril design could help design future optimal fibrils with less help from human intuition.**

## 1. Introduction

Geckos can climb almost any surface in nature swiftly and effortlessly. Such incredible climbing ability comes from the hair-like microstructures, setae, on their feet.[1] The setae branch into many smaller hairs of seta with a spatulated tip ending, where these tips directly contact and adhere to surfaces leveraging mainly the most universal intermolecular force, van der Waals forces.[2,3] The hierarchical and branching fibrillar structure of setae enables exploiting contact splitting and crack trapping and adhesion to even rough surfaces.[4,5] Such fascinating adhesion evoked an inspiration for a synthetic elastomeric gecko pad.[6] The research on synthetic gecko pad resulted in many follow-up studies on dry fibril adhesives, such as contact splitting and crack trapping,[7] adhesion controllability,[8–10] self-cleaning property,[11–13] hierarchical structuring,[14,15] multi-material composite fibrils,[16–18] adhesion with any liquid super-repellency,[19] adhesion to skin,[20–22] soft robotic grippers,[23,24] and robotic wall climbers.[25–27]

The adhesion strength of synthetic gecko fibril arrays is studied typically on smooth surfaces, and it is a function of the size and shape of the fibril tip and stem in addition to the fibril density, fibril elastomeric material properties, and the fibril array backing layer. For a single fibril, the adhesion strength is especially sensitive to the geometry of the fibril structure.[28–32] It is found that the tip geometry is crucial to the adhesion improvement, where bioinspired mushroom-[33–40] and T-shaped[41,42] fibril tips improved the adhesion strength notably greater than the one from simple flat-punch fibrils, and subsequently multiple optimal mushroom- and T-shaped tip geometries have been proposed in the literature.[33,41–43] Additionally, not only the tip shape but also the neck and body shape of a fibril affect significantly the stress profile at the adhesion interface and the tip edge singularity by changing the boundary condition for (un)loading problems, thus the optimization of the shape of the fibril has been an active research topic to enhance the adhesion of fibrils.[28,33,42,43]

Limitations arise when optimizing such previously proposed tip shapes due to the nature of the current template-based design approach. Such approach is based on a pre-determined T- or mushroom-shaped tip with a cylindrical stem, and suppresses the chances to explore and find out-of-the-box optimal tip and stem shapes. To resolve this limitation, here we

Prof. D. Son
School of Mechanical Engineering
Pusan National University
Busan 46241, South Korea
Prof. D. Son, Dr. V. Liimatainen, Prof. M. Sitti
Max Planck Institute for Intelligent Systems
70569 Stuttgart, Germany
E-mail: sitti@is.mpg.de
Dr. V. Liimatainen
Okmetic Oy
Vantaa 01510, Finland
Prof. M. Sitti
Institute for Biomedical Engineering
ETH Zurich
Zurich 8092, Switzerland
Prof. M. Sitti
School of Medicine and College of Engineering
Koç University
Istanbul 34450, Turkey
The ORCID identification number(s) for the author(s) of this article can be found under https://doi.org/10.1002/smll.202102867.

© 2021 The Authors. Small published by Wiley-VCH GmbH. This is an open access article under the terms of the Creative Commons Attribution License, which permits use, distribution and reproduction in any medium, provided the original work is properly cited.

**DOI: 10.1002/smll.202102867**

propose a machine learning (ML)-based computational design approach, where the 3D tip and stem shape of an adhesive fibril is searched in a broad design space and optimized automatically at a given fibril diameter scale and material.

ML-based design optimizations have been widely used in various areas, such as optimal antenna design,[44] composite design,[45–48] mechanical property prediction,[49,50] polymer dielectrics,[51] aircraft airfoil design,[52] mechanical structure design,[53] and energy materials.[54] Most of these studies rely on approximate models of finite-element-method (FEM)-based simulations by training artificial-neural-networks (ANNs) in order to accelerate the simulation evaluations. Improved evaluation speed of the approximated models makes the global optimization methods, such as genetic algorithms, feasible. However, the main drawbacks of such approach are high computational time and cost to create the training dataset for the ANNs and lower accuracy due to the approximation process.

Here, we propose a ML-based adhesive fibril design method with a data-efficient optimization framework and accurate FEM-based adhesion mechanics simulations. By employing a state-of-the-art global optimization method, Bayesian optimization,[55–60] with comprehensive FEM-based adhesion mechanics simulations, the proposed method produces optimal shapes of fibrils, which outperform previous adhesive fibril designs in both simulations and experiments. Compared to a recently proposed ML approach for adhesive fibril design,[61] this study provides the first experimental validation of fibrils designed by ML methods together with in-depth stress analyses. In addition, our proposed method is much more data efficient to generate a sub-optimal design in a reasonable duration (≈3 h for each design in this study) and flexible for the changes in the simulation, where the governing physics of the simulation could be readily changed without any prior training of a model, allowing the creation of different adhesive fibrils with other adhesion mechanisms, such as suction. Finally, our method also optimizes the fibril 3D stem shape and deformation in addition to the tip shape, which is ignored in almost all previous template-based and in the previous ML-based fibril optimization method.

## 2. Results and Discussion

### 2.1. Fibril Designs

The proposed computational single fibril design framework has two components: FEM-based adhesion mechanics simulation and Bayesian optimization[55–60] (**Figure 1**a). During the design

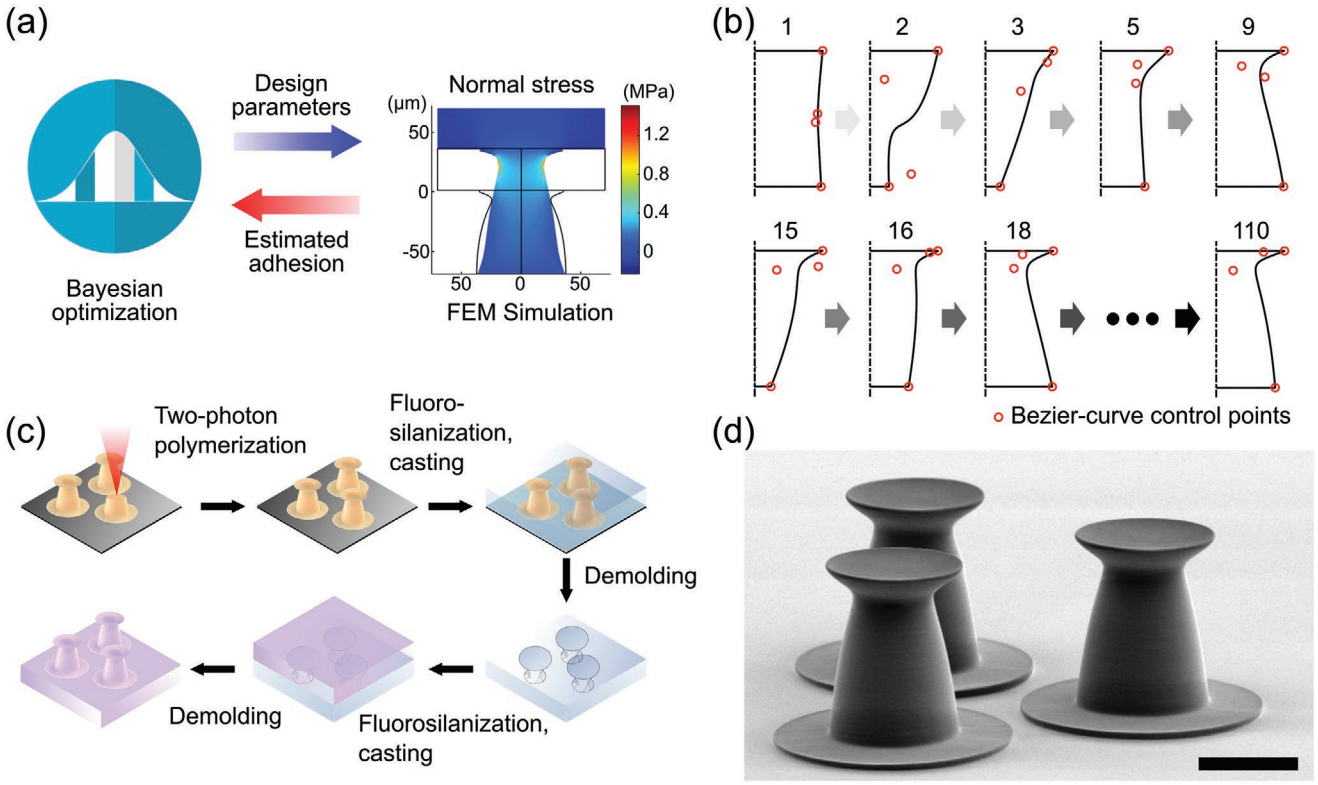



**Figure 1.** Design and fabrication process of the machine learning-based design of fibrils (MLFs) for maximal adhesion on smooth flat surfaces. a) A design optimization goal (e.g., maximize adhesion) along with the design constraints is supplied to the Bayesian optimization algorithm. The Bayesian optimizer provides design parameters to the simulator, and the simulator returns the estimated adhesion back using a finite element method (FEM)-based adhesion mechanics simulation. This process runs iteratively until the optimal design is achieved. b) The algorithm starts with a random shape and explores the broad design space by controlling Bezier-curve control points to maximize the estimated adhesive force from the FEM simulation. In each iteration, a comprehensive FEM simulation from the initial attachment to the detachment is performed. As the iteration number increases (the numbers in (b)), the shape evolves to the best design. c) After the optimization, the best design is fabricated using two-photon polymerization and a subsequent double molding-based replication technique. d) The fabricated version of the optimal fibril design with the tip diameter of 70 μm (iteration number 110 at (b)) is shown in a scanning electron microscope (SEM) image (the scale bar indicates 50 μm). The fibrils are made of polydimethylsiloxane (PDMS) elastomer.


© 2021 The Authors. Small published by Wiley-VCH GmbH

process, the optimizer generates design parameters for the simulation, whereas the simulator returns an estimated adhesive force based on the design parameters from the optimizer. This process runs iteratively until a preset iteration limit, and the optimizer returns the optimal design parameters based on the observations along the design process.

In the simulation, the shape of the fibril is constructed by design parameters with the following assumptions. First, the fibril is assumed to be axisymmetric and the attached surface is assumed to be smooth and locally flat, as in the case of typical T- and mushroom-shaped fibril designs. Additionally, the aspect ratio of the fibril is set to be 1:1 in order to compare the fibril with other fibril designs at the same aspect ratio, which removes the effect of having different aspect ratios on adhesion tests.[34] Next, the side profile of the fibril is constructed by a Bezier curve,[62] which connects the top edge of the fibril to the base of the fibril smoothly with a given number of control points (Figure 1b). In this study, we use a third order Bezier curve to represent the fibril's profile including its tip and stem, however, the order of the curve could be adjusted. We show the effect of the order of a Bezier curve used to represent the fibril profile on adhesion in the supplementary material (Figures S1 and S2, Supporting Information). Note that it is critical to keep the order of the Bezier curve as low as possible to avoid the overfitting problem.[63] Finally, the simulation takes the fabrication constraints into account, where an infinite sharp edge is not possible to fabricate in practice. Therefore, the edge of the tip is rounded by a certain fillet radius, estimated from the experimental fabrication test results by the two-photon-polymerization-based direct 3D microprinting technique and subsequent double molding processes used in this study.

Once the shape of a fibril is determined at a given iteration step, the adhesion of such fibril is simulated in a FEM simulation environment. Here the simulation considers nonlinear deformation of a fibril during adhesion tests by incorporating the Mooney–Rivlin hyperelastic model,[64,65] and a realistic detachment of the fibril from a flat-punch probe using a Dugdale–Barenblatt cohesive zone model.[34,66,67] This approach reflects changes of the stress profile during the fibril stretch and right before the detachment of the fibril, which results in a direct adhesion value estimation rather than the previous indirect adhesion estimation based on a fixed interfacial stress profile.[41,42] Assuming that the fibril tip is contacted to a smooth flat-punch probe fully, the adhesion is calculated by integrating the normal stress on the surface of the base of the fibril. When the fibril is stretched due to the tip adhesion, the hyperelastic model predicts the deformation of the tip and the stem. When a crack forms at the tip-substrate contact interface due to a normal stress exceeding the interfacial theoretical strength,[34,68] the adhesion quickly reaches its maximum and decays subsequently.[33] Here, the material properties and fabrication constraints determining the achievable edge sharpness are characterized experimentally and calibrated before the design of the fibrils (see Methods for the details).

The simulation framework is directly linked to a Bayesian optimization framework. Bayesian optimization is a state-of-the-art global optimization method[55–57] for problems where it is vital to optimize a performance criterion while keeping the number of evaluations of the system small.[69] This method becomes an ideal candidate for our problem by minimizing the number of FEM-based adhesion evaluations without compromising the simulation accuracy. Here, the optimization goal is to maximize the adhesive force. The optimizer takes the Bezier-curve control points as optimizable variables and reaches the optimal design in each iteration number (Figure 1b). The other parameters, such as the tip diameter and the fabrication constraint-related edge sharpness limit, are preset before the optimization. Note that the proposed method is flexible to take other types of optimization goals, such as maximizing adhesion energy at the interface (see Methods for the details).

Here, the previous ML-based adhesive fibril design study[61] could be compared with ours. The previous study used a trained deep-neural-network (DNN), which simulates the adhesion profile at the interface. The differences lie in the simulation accuracy and data efficiency. First, the DNN-based approach does not compute the adhesion directly from the simulation, rather it estimates the adhesion indirectly with an infinitesimal fibril stretch. This approach would not be accurate when the fibril is deformed due to the elasticity of the material, where the stress profile drastically changes. Soft elastomers, such as polydimethylsiloxane (PDMS) used in our experimental fibrils and in all previous T- and wedge-shaped mushroom fibril studies, do stretch significantly during the pull-off process resulting in the hyperelastic regime.[19] In contrast, our method estimates adhesion directly right before the detachment considering the hyperelastic body deformation of the fibrils. Second, our method is data efficient by orders of magnitude more than the DNN-based approach. More specifically, our method allows to find an optimal shape within 150 function evaluations, whereas the DNN-based method requires more than 200 000 function evaluations to create training dataset. Furthermore, the DNN-based approach is not flexible because a single change in the simulation might require another whole set of data causing a significant computational time.

Once the optimal fibril design is obtained, such fibril is fabricated using two-photon polymerization (2PP) process and a subsequent double-molding-based replication technique (Figure 1c).[19] This fabrication method is versatile to create various shapes as well as allows the use of various elastomeric materials. We chose PDMS as our fibril material because it is commonly used in the dry fibrillar adhesion field, versatile, flexible as well as it exhibits less surface energy, less environmental sensitivity, and less viscoelastic effects compared to other fibril elastomers, such as polyurethane.[13,70,71] First, computer-aided-design (CAD) files of the fibrils are 3D-printed using a high-resolution rigid photoresist using 2PP to create a master template, and then fluorosilanized to allow easy replication. Afterward, PDMS is casted on the master template to form a negative replica, cured, peeled off, and then fluorosilanized. Finally, the fluorosilanized PDMS negative mold is replicated again to create a PDMS fibril replica of the original master (Figure 1d).

With the proposed design framework, the ML-based optimally designed fibrils (hereafter MLFs) with various tip diameters (30, 50, 70, 90 μm) are designed and fabricated (Figure 1d and Figure S3, Supporting Information). We create two types of MLFs based on the interfacial stress type which causes a failure: $MLF_n$ based on normal stress failure and $MLF_v$ based on von-Mises stress failure at the interface.


© 2021 The Authors. Small published by Wiley-VCH GmbH

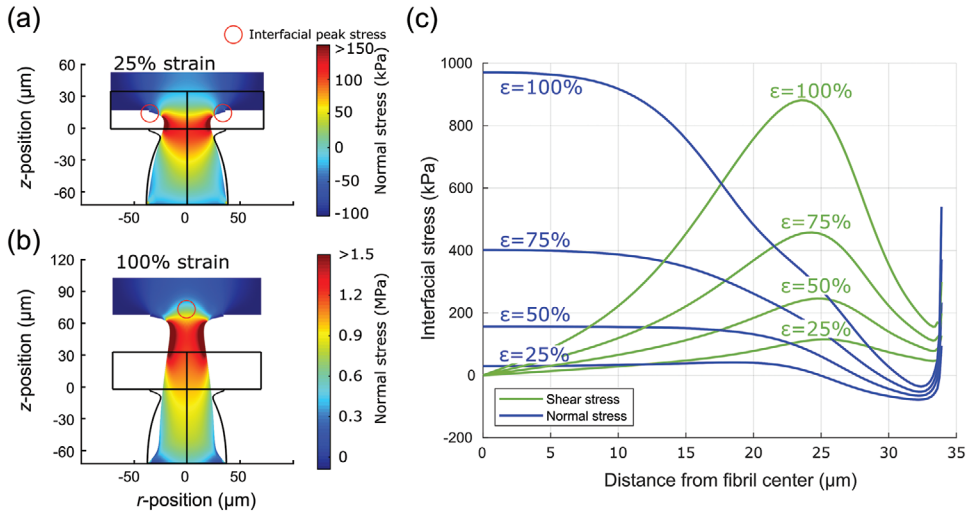



**Figure 2.** Stress profile changes by the fibril stretch in FEM simulations for a 70 μm-diameter $MLF_n$. a) When the fibril is stretched by a small amount (25% strain), the peak stress on the fibril tip surface occurs at the tip edge. b) However, when the fibril is stretched by a large amount (100% strain), the normal peak stress occurs at the center, rather than the edge. Also, the stress pattern throughout the fibril stem changes indicating that the stem deformation changes the way the stress is transferred to the tip-surface contact interface. c) The evolution of the tip-surface interfacial stress profile explains the change of the peak stress where the stress at the center increases rapidly than the stress at the edge by stretching. Comparable results of $MLF_v$ are shown in Figure S5, Supporting Information.

Here $MLF_v$ helps us understand the role of the shear stress to adhesion by comparing it with the result of $MLF_n$. The critical simulation parameters, such as the fabricable sharpest edge radius, hyperelastic model parameters, and the theoretical adhesion strength of the contact interface are experimentally measured and updated in the simulation before the design optimization.

The MLFs result in unique stem and tip shapes compared to the previous fibrils. The shape of the MLFs features a sharp tip edge with a large wedge, a narrow neck, and a thickening body toward the base of the fibril (Figure 1d and Figure S3, Supporting Information). The optimization process seems to capture the tip edge singularity[72] by creating sharp tip edges. This makes the tip geometry rather similar to the other fibrils. However, the significant differences are found in the neck and stem shapes. Here, as the narrow neck and the thickening stem help reduce stress concentration at the tip edge when the fibril is stretched by transferring most of the stress to the center of the fibril tip. Compared to the previously reported narrow neck designs[38,43] to minimize any misalignment errors,[73] these new designs utilize the stem deformation to alter stress profile at the interface along the stretch of the fibril (see **Figure 2**a,b with the details given in the following section).

Besides the adhesion-force-optimized MLFs ($MLF_n$s), adhesion-energy-optimized MLFs ($MLF_e$s) could be considered. By replacing the optimization goal of adhesion force maximization by adhesion energy maximization, the algorithm creates MLFs with maximum adhesion energy (Figure S4a, Supporting Information). The energy optimized fibrils present narrower stem body to increase the adhesion energy rather than having short displacement distance with higher forces (Figure S4b,c, Supporting Information). Our simulation results show comparative adhesion tests among these two types, showing that adhesion energy optimized fibrils show higher adhesion energy while demonstrating compromised maximum adhesion forces.

### 2.2. Stress Profile Changes during Stretching a Fibril

The finite element analysis on the interfacial stress and fibril stretch (Figure 2) reveals that the stress profile changes greatly during stretching a fibril. More importantly, the location of a peak stress changes from the edge of the tip to the center of the tip due to the stem deformation. This fact suggests that the design of an adhesive fibril should consider stress profiles not only at the beginning of the tip detachment (which is the case in ref. [61]), but also at during all detachment processes due to the deformation of the fibril tip and stem.

In case of $MLF_n$ (70 μm tip diameter), when a fibril is insignificantly stretched (25% strain in Figure 2a for $MLF_n$ and Figure S5a, Supporting Information for $MLF_v$), the stress pattern throughout the body forms a convex gradient pattern. More importantly, the peak stress occurs at the edge of the fibril tip (Figure 2a,c). However, this peak stress is not enough to form a crack to initiate detachment of the fibril tip from the probe with this amount of strain. When the fibril is stretched significantly (100% strain in Figure 2b for $MLF_n$ and Figure S5b, Supporting Information for $MLF_v$), the stress pattern in the stem changes due to the deformation. The stress gradient in the stem forms a concave pattern now (Figure 2b,c and Figure S5b,c, Supporting Information for $MLF_v$). The most critical part is the change of the location of the peak stress; it occurs at the center of the interface compared to the edge at the beginning, which means that the stress singularity at the beginning might not be critical for fibrils that experience such large deformations. Furthermore, the stress profile reveals that $MLF_n$ reached 46% of the theoretical


© 2021 The Authors. Small published by Wiley-VCH GmbH

maximum by calculating the fraction of the area under the normal stress profile over the full circular area composed of the theoretical interfacial strength and the tip diameter.

While the previous simulation studies assume that the adhesive fibril does not change shape during the pull-off[36,42,61] or deforms very small staying in a linear deformation regime,[33] this result indicates that hyperelasticity must be considered for adhesion simulations when the fibril is made of soft elastomers, such as PDMS,[74] which stretches significantly during the pull-off process.

### 2.3. Fabrication Constraints Impact the Optimal Design and Adhesion

The fabrication constraints worsen the adhesion performance due to the edge singularity[75] induced by a rounded edge.[76] Our design methodology reflects such fabrication constraint, where it changes the optimal shape to cope with the edge singularity. To understand how a fabrication constraint changes the optimal design proposed by the algorithm, a set of design optimizations is performed. The edge fillet radius, $r_e$, (not the radius of the fibril) is chosen as a control variable, and the algorithm performs design optimizations for each $r_e$. Here we set the fibril diameter as 70 µm as a representative case.

Our simulation analysis suggests that the fabrication constraint greatly impacts the optimal shapes of the fibrils, showing that such constraints must be considered in the design processes. When such constraint is negligible compared to the size of the fibril, the optimal shape shows sharp edge with relatively thick neck and stem (**Figure 3**a). The upper part of the body is very close to the wedge-shaped fibrils,[33] showing an agreement with previous analysis on the shape of the fibrils. The design changes when the fabrication constraint becomes non-negligible. As the constraint increases, the fibril tends to show much narrower neck compared to the designs with less constraint. Also, the body shape changes by having a narrower body. These could be interpreted as to minimize deformation at the top body, by transferring most of the deformation to the lower body, which might reduce the risk of increasing stress peak at the tip-surface interface. Nonetheless, as the constraint increases, the adhesion deteriorates multifold due to the increased peak stress at the edge. Additionally, we provide the analysis on the effect of the size of the fibril tip with a given fabrication limit, where such fabrication limit affects the optimal shape similar to above analysis (Figure S6, Supporting Information). The proposed design framework generates different optimal fibril shapes for different fabrication limits and tip sizes.

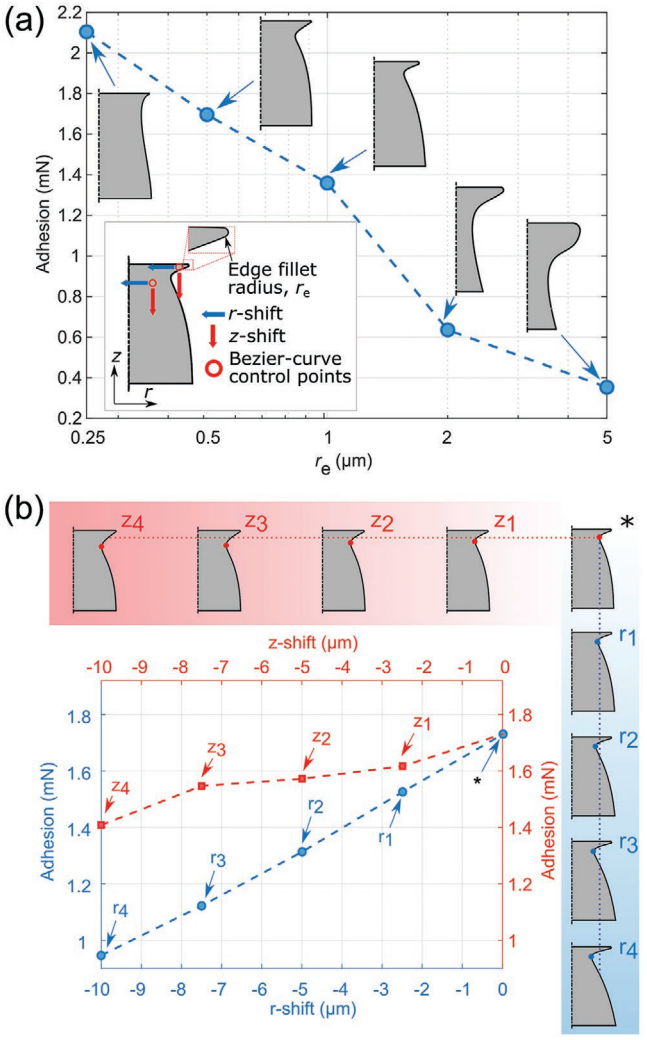



**Figure 3.** Sensitivity analysis of adhesion as a function of the fabrication constraint and the stem shape in FEM simulations. a) The optimal design changes by the fabrication constraint, that is, the tip sharp edge curvature, $r_e$. When the fabrication constraint is minute ($r_e$ = 0.25 µm), the predicted optimal design is similar to the wedge-shaped fibrils, such as the optimal design predicted by refs. [33] and [61]. When the fabrication error is significant to the size of the fibril, the optimal fibril shape changes by having a narrow neck and stem. Subsequently, the performance of the fibrils deteriorates with the increased $r_e$. b) The stem shape change based on radial control points (*r*-shift) of the Bezier-curve affects the simulated adhesion performance significantly (blue dotted line). The stem shape change based on axial control points (*z*-shift) affects the adhesion performance less significantly (red dotted line).

### 2.4. Fibril Body Shape Sensitivity in the Fibril Adhesion Performance

The effect of the fibril body shape is further analyzed to understand its role in the fibril adhesion. It is found that the adhesion significantly depends on the fibril stem shape, whereas most of the previous studies focused only on the tip geometry.[77] 70 µm $MLF_n$ is chosen (marked as * in. Figure 3b) as the base design and the two Bezier control points which form the profile are modulated in radial and axial manner (*r*- and *z*-direction in the inset of Figure 3a) in simulations. The other Bezier control points at the ends of the curve are fixed.

The change in the radial control points shows high sensitivity in the adhesion performance. As the radial control points move toward the axis, the neck shape gets narrower resulting in the change of the curvature of the lower body, while the general wedge shape remains steady. This change of the stem shape is directly reflected in the adhesion, by having lower adhesion with a thinner stem (Figure 3b, blue line). On the contrary, the


© 2021 The Authors. Small published by Wiley-VCH GmbH

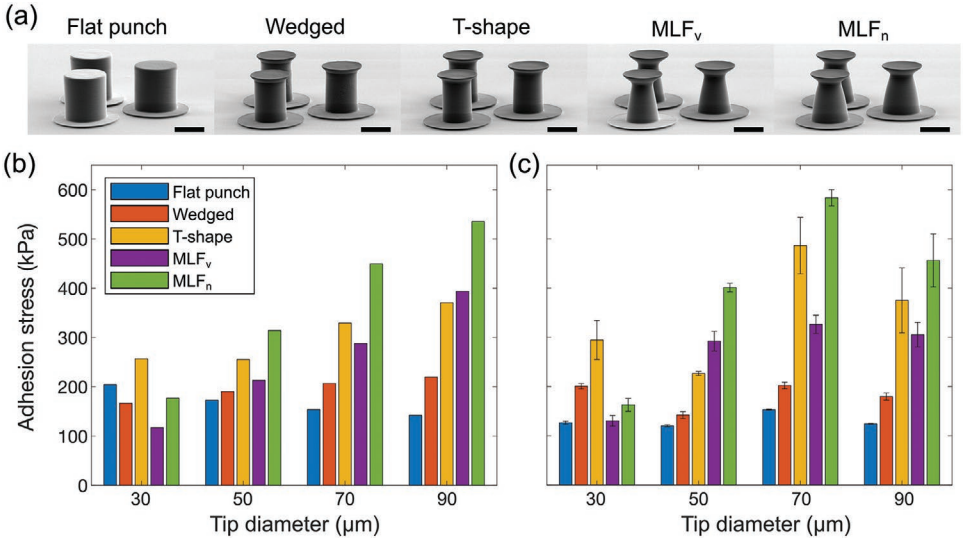



**Figure 4.** Adhesion test results in simulations and experiments. a) The fabricated MLFs and reference designs with 70 μm tip diameters are shown in SEM Images (the scale bar indicates 50 μm; fibrils with different diameters are found in Figure S3, Supporting Information). b) The FEM simulation predicts that MLF$_n$ has overall superior adhesion performance compared to the other designs. On the contrary, MLF$_v$ has lower adhesion than MLF$_n$ and T-shaped fibrils suggesting that the design criteria for MLF$_n$ are effective to the adhesion improvement than the one of MLF$_v$. c) The experimental results confirm that the adhesion performance improvement of MLF$_n$ and shows an overall agreement between the simulations and experiments.

axial control points affect the adhesion less than the radial control point shifts (Figure 3b, red line), which change the height of the neck, while keeping the body thickness similar. The interfacial stress analysis of these variants (Figure S7, Supporting Information) shows smaller area under the normal stress profile than the original MLF$_n$ optimal design, explaining the decreased adhesion of these variants. Note that the adhesion is the surface integral of the normal interfacial stress, which is directly related to the area under each stress profile. Here, the reason why some direction affects more than the other is rather complex and unclear, but it is important to note that the shape of the body affects the adhesion by transferring the stress from the base to the tip as shown in Figure 2. The stem shape sensitivity shown here suggests that it is important to consider the stem shape in the design optimization, which has not been well highlighted in the previous studies. Additional to those, top surface shape of the fibril affects the adhesion as suggested in ref. [28]. Our additional simulation study suggests that concave shape of the top surface resulted in a dramatic decrease of the adhesion, which is the worst-case scenario in dry adhesion optimization due to the increased edge singularity (Figure S8, Supporting Information). On the other hand, the MLF$_n$ is robust to the convex tip shape as it does not cause direct edge singularity. Nonetheless, the MLF$_n$s are optimized for the flat tip surface and show the optimal performance with the flat tip interface similar to all previous fibril adhesion optimization studies.

### 2.5. Adhesion Performance of the Fabricated Optimal Fibrils

We create a triplicate of each design forming a tripod for accurate alignments with a smooth spherical glass probe (the diameter of the probe (8 mm) is much larger than the diameter of the fibril (≈30–90 μm); therefore, a flat-flat contact interface can be assumed locally), while keeping the number of fibrils minimum to reduce the effect of multiple fibrils on a soft backing layer (**Figure 4**a and Figure S3, Supporting Information).[78] Previously reported fibril shapes are also fabricated to compare their adhesion as controls/references. A flat-punch fibril,[6,32,68] wedge-shaped mushroom fibril,[33,79] and modified T-shaped fibril, which has a fillet radius between the fibril and the cap,[80] are our references because those are well-understood, widely adopted, and optimal designs developed in the literature so far. Additionally, due to the fabrication limitation, the ML-based optimal fibril[61] is compared in our simulation framework with the other control and MLF fibrils (Figure S9, Supporting Information).

Figure 4b,c shows comparative adhesion measurements of the fibrils in simulations and experiments. First of all, adhesion improvement is observed in MLF$_n$ for most of the tip diameters (50, 70, 90 μm, except 30 μm) compared to other designs. MLF$_n$ shows 77% adhesion improvement over modified T-shaped fibril with the size of 50 μm tip diameter in the experiment. Compared to MLF$_n$, the MLF$_v$ does not show great adhesion performance, indicating that the shear stress minimization at the interface does not affect the adhesion performance positively. This could be explained comparing the stress profiles of MLF$_n$ and MLF$_v$, where MLF$_v$ has lower shear stress along the stretch (Figure 2c and Figure S5c, Supporting Information). A previous study points out that shear stress helps the normal adhesion, which partially supports this result.[81] In the small (30 μm) tip diameter case, MLFs show worse adhesion compared to the other designs. A relatively large edge radius and a large wedge (Figure S3, Supporting Information) show that the algorithm fails to minimize the edge singularity. In general, the predicted adhesion shows agreement with the experiments. In most of the cases the trend is captured, where the flat-punch fibrils show the lowest and the MLF$_n$ fibrils show the highest followed by T-shaped fibrils.


© 2021 The Authors. Small published by Wiley-VCH GmbH

Fibrils with large deformations tend to show large standard deviation within the first five measurements of adhesion indicating Mullin's effect (compare standard deviations in Figure 4c and the maximum strains of Figures S10 and S11, Supporting Information).[82] This effect does not affect significantly for the simple applications such as fasteners or adhesive designs, however, may pose limitations in applications such as MEMS assembly or electronics handling which requires thousands of loading and unloading cycles.[83]

$MLF_n$ fibrils show overall superior adhesion compared to the previously proposed machine learned fibrils[61] in two sets of simulation experiments (Figure S9, Supporting Information): 1) fibril design using the extreme edge sharpness[61] and 2) applying our fabrication limit, which was applied to MLF fibrils. In smaller sizes, the previously proposed fibrils[61] showed superior adhesion compared to the other fibrils leveraging nanoscale edge sharpness, while the other fibrils did not benefit from such reduced fabrication limitation. Even with that, in large diameters, the previously proposed fibrils[61] become inferior to $MLF_n$ fibrils. Second, by applying all the same fabrication limits as the other fibrils (rounded edge with 1 µm fillet radius),[61]s fibril shows weaker (around half of $MLF_n$ fibrils) adhesion.

## 3. Conclusions

This study proposes a design framework and experimental verification of adhesive fibrils based on Bayesian optimization and FEM-based adhesion mechanics simulations. Unlike previous approach based on bio-inspiration and human intuition, our ML approach discovered novel optimal designs and improved the adhesion performance significantly in simulations and experiments. For the adhesion simulation, the hyperelasticity is incorporated in the FEM simulation for the first time predicting the adhesion close to the experiments. The design optimization framework allows the use of comprehensive and accurate adhesion simulations in concert with Bayesian optimization, generating optimal shapes of fibrils in various diameters and various fabrication limits. Further analyses provide evidences that 1) the large axial stem deformation causes the fibril tip stress profile change, 2) fabrication constraints are important to be incorporated in the design process, and 3) fibril stem shape is also important to the adhesion performance. The proposed fibril design method could help design optimal future fibrils with less help from human intuition.

## 4. Experimental Section

*FEM Simulations*: The FEM simulation was designed to estimate adhesion based on the design parameters (Figures 1a, 3, 4b, and Figure S9, Supporting Information) and to analyze the tip stress profile (Figure 2 and Figures S4, S5, S7, S9, Supporting Information). Using a commercial FEM tool (COMSOL Multiphysics 5.4, COMSOL Inc.), the interfacial stress distribution and the maximum adhesion were estimated based on the approach of ref. [33] with a modification by implementing the Mooney–Rivlin five-parameter hyperelastic model of the material.[64,65] During the simulation, the fibril's base was fixed and the tip of the fibril was initially attached to a flat-punch probe. The position of the probe was then iteratively translated to impose stretch to the fibril. The simulation terminated itself when the maximum interfacial normal stress reached the theoretical interfacial strength.

Material characterization experiments were performed before the simulation. This was because soft elastomer (PDMS) fibril might behave differently in small scales than in bulk in terms of mechanical properties. For this calibration, first, different shapes of fibrils (flat punch, wedge-shaped, T-shaped in 30, 50, 70, 90 µm diameter) were fabricated using with 2PP and double-molding-based replication method (Figure 1c). Afterward, adhesion and force–displacement curves were measured to calibrate the Mooney-Rivlin five parameters and theoretical interfacial strength. Specifically, the theoretical interfacial strength value was achieved by matching the adhesion simulation and the characterization experiments. The value which minimized the root-mean-squared relative error of all shapes was chosen as the final theoretical interfacial strength for designing the MLFs. The final value achieved with the fabrication process in this paper was 966 kPa. Additionally, by taking scanning electron microscope images of the fibrils, the fabrication constraint (the tip edge fillet radius) was characterized.

A shape of a fibril was determined by two sets of parameters: fixed parameter set and optimizable variable set. The fixed parameter set included aspect ratio, tip diameter, edge fillet radius, the Mooney-Rivlin parameters, and the theoretical interfacial strength. The optimizable parameter sets included two Bezier control points and the fibril base diameter. The geometry of the fibril was axisymmetric. Once the shape was determined, a fibril was meshed with more than 10 000 triangular elements, with extremely fine meshes toward the edge of the fibril to handle the interfacial stress singularity.

*Bayesian Optimization*: Once the FEM simulation was constructed, the optimizable variable set, $\boldsymbol{x}$, was directly handled by the Bayesian optimizer to produce the optimal adhesive fibril. Here, $\boldsymbol{x}$ was a 5D vector including two Bezier control points in *r*- and *z*-coordinate, and the diameter of the fibril base. The optimization problem was formulated as

$$\boldsymbol{x}^* = \underset{\mathbf{x}}{\operatorname{argmax}}\, f(\boldsymbol{x}, \boldsymbol{p}), \text{subject to } \boldsymbol{x}_{\min} < \boldsymbol{x} < \boldsymbol{x}_{\max} \tag{1}$$

where $f(\cdot)$ is the estimated adhesive force from the simulation, $\boldsymbol{x}^*$ is the optimal variable set, $\boldsymbol{p}$ is the fixed parameter set, $\boldsymbol{x}_{\min}$ is the lower bound of $\boldsymbol{x}$, and $\boldsymbol{x}_{\max}$ is the upper bound of $\boldsymbol{x}$. This optimization problem was solved with a prebuilt Bayesian optimization function (bayesopt.m) in a proprietary programming language (MatLAB R2020a, The MathWorks, Inc.) with the expected improvement acquisition function. In the problem, the adhesion converged within 150 iterations.

Additionally, to create other types of fibrils with other design goals, the objective function for the Bayesian optimization could be changed. To maximize adhesion energy, the optimization problem was formulated as

$$\boldsymbol{x}^* = \underset{\mathbf{x}}{\operatorname{argmax}} \int_0^{h^*} f(\boldsymbol{x}, \boldsymbol{p}, h)\, dh, \text{subject to } \boldsymbol{x}_{\min} < \boldsymbol{x} < \boldsymbol{x}_{\max} \tag{2}$$

where $h$ is the displacement of the tip of the fibril during the adhesion test, and $h^*$ is the maximum displacement when the fibril was separated from the adhesion indenter tip. Here the integration of the adhesion force along the displacement of the tip of the fibril indicated the adhesion energy of the fibril.

The communication between the optimizer and the simulator was established via LiveLink (COMSOL Multiphysics 5.4, COMSOL Inc.). The total of 150 iterations combined with optimization and simulation took less than 3 h to produce the final design of the fibrils using a performance desktop computer (20 cores of Intel Xeon CPU E5-2680 v2, 2.80 GHz (40 logical cores), 192 GB RAM, NVIDIA Quadro K5000 graphics card). The process of the Bayesian optimization and convergence is shown in Figure S12, Supporting Information.

*Fibril Fabrication*: The fabrication process was similar to the fabrication method presented in ref. [19] with modification in the fabrication parameters for sharper edge definitions. First, the fibrils were designed using a CAD software (SolidWorks 2020, Dassault


© 2021 The Authors. Small published by Wiley-VCH GmbH

Systèmes Co.), and then converted to a 2PP raster file (DeScribe, Nanoscribe GmbH), and printed using a 2PP 3D microprinter (Photonic Professional GT, Nanoscribe GmbH). The masters were printed on an indium tin oxide (ITO)-coated glasses using a rigid IP-S commercial photoresist (Nanoscribe GmbH). To enhance the adhesion between the ITO-coated glass and the fibrils to be printed, the ITO-coated glass was exposed to 1,1,1,3,3,3-hexamethyldisilazan (HMDS) in a desiccator more than 6 h before the 3D print. Afterward, the master was developed in propylene glycol monomethyl ether acetate (PGMEA, Sigma Aldrich Inc.) for 40 min and rinsed in isopropyl alcohol (IPA) for 3 min. After the master fibril array (4 × 5) was fabricated, the array was exposed to ozone plasma (ozone plasma chamber, Zepto, Diener electronic GmbH) in 80 °C for 30 min for surface activation, and subsequently placed in a vacuum desiccator with a glass vial containing 0.1 mL of trichloro (1H, 1H, 2H, 2H-perfluoroctyl) silane (Sigma Aldrich Inc.) for 35 min. Finally, the master was placed in 90 °C oven for 35 min.

Degassed PDMS mixture (20:1 monomer to crosslinker ratio) was casted on top of the fluorosilanized master array and degassed for 30 min in a vacuum desiccator. Then the master and the cast were baked in a 90 °C oven for 35 min. Afterward, the negative mold was peeled off. To silanize the negative mold, a similar procedure was applied. The negative mold was exposed to ozone plasma in 80 °C for 30 min, and placed in a vacuum desiccator with trichlorosilane for 40 min. Afterward, the negative mold was baked in 65 °C for 3 h. After the negative mold was peeled off, PDMS mixture (10:1 monomer to crosslinker ratio) was casted on top of the negative mold, degassed for 30 min, and cured for 3 h in a 65 °C preset oven. The positive replica was ready after peeled off from the negative mold. The surface roughness of the fibril surface was $R_q$ of 0.42 µm with cutoff frequencies of $\lambda_s$ = 0.25 µm and $\lambda_c$ = 0.25 mm. Young's modulus of PDMS (65 °C cured for 3 h) was 1.6 MPa. As the material behaved different at the microscale, adhesion test of the T-shape fibril (Figure S10c, Supporting Information) was used to as the baseline stress–strain curve to fit a hyperelastic model (Mooney-Rivlin fifth order model) for the simulation framework due to the known shape and relative strong adhesion compared to other fibril shapes. The fifth order Mooney–Rivlin parameters were $C_{10}$ = −1.81e+06 Pa, $C_{01}$ = 3.04e+06 Pa, $C_{20}$ = 9.82e − 09 Pa, $C_{02}$ = −1.52e+05 Pa, $C_{11}$ = 6.83e+05 Pa.

*Adhesion Measurements*: The adhesion of the fibrils was tested in a customized adhesion setup. A load cell (GSO-25, Transducer Techniques LLC) was attached to a vertically moving (axial direction to the fibrils) high-precision motorized piezo stage ("LPS-65 2," Physik Instrumente GmbH) with 5 nm positioning resolution. Horizontal positions (*xy*-position) were adjusted by manual *xy*-stage with an additional motorized piezo stage. The motion control of the motorized stages and the force measurement from the loadcell were performed simultaneously in a custom-built program in LabVIEW environment (National Instruments Co.) with 1 kHz data acquisition rate. The raw data was filtered to reduce noise with 10 points median filter. An inverted optical microscope (Axio Observer A1, Carl Zeiss AG) was placed under the setup to visualize the contact interface for alignments and adhesion analyses.

A spherical smooth glass probe with a diameter of 4 mm was used as an indenter directly connected to the load cell. The surface roughness of the glass probe was Rq of 1.04 µm with cutoff frequencies of $\lambda_s$ = 0.25 µm and $\lambda_c$ = 0.25 mm. The *xy*-position of the probe was carefully adjusted to place the probe at the center of the triplicate of the fibrils. The approach and retraction speeds were 10% of the fibril size per second (e.g., 7 µm $s^{-1}$ for 70 µm fibril) to minimize the viscoelastic effects. The probe indented until it reached a certain preload (150 kPa for all sizes, e.g., 0.577 mN for 70 µm tip diameter fibril), waited for 30 s for the relaxation, and was retracted (Figure S11, Supporting Information). The adhesion was measured together with displacement to form force–displacement curves (Figure S10, Supporting Information). The measurements were performed five times per each design and the adhesion was estimated as the average of the measured adhesion per fibril. Because the multiple fibrils were detached, multiple spikes in the adhesion curves were observed (Figures S10 and S11, Supporting Information).[78]

## Supporting Information

Supporting Information is available from the Wiley Online Library or from the author.

## Acknowledgements

This work was funded by the Max Planck Society.
Open access funding enabled and organized by Projekt DEAL.

## Conflict of Interest

The authors declare no conflict of interest.

## Data Availability Statement

The data that supports the findings of this study are available in the supplementary material of this article.

## Keywords

adhesion modeling, adhesive fibrils, computational design, gecko adhesion, machine learning

Received: June 23, 2021
Published online: August 19, 2021

[1] R. Ruibal, V. Ernst, *J. Morphol.* **1965**, *117*, 271.
[2] K. Autumn, M. Sitti, Y. A. Liang, A. M. Peattie, W. R. Hansen, S. Sponberg, T. W. Kenny, R. Fearing, J. N. Israelachvili, R. J. Full, *Proc. Natl. Acad. Sci. U. S. A.* **2002**, *99*, 12252.
[3] K. Autumn, Y. A. Liang, S. T. Hsieh, W. Zesch, W. P. Chan, T. W. Kenny, R. Fearing, R. J. Full, *Nature* **2000**, *405*, 681.
[4] J. Y. Chung, M. K. Chaudhury, *J. R. Soc., Interface* **2005**, *2*, 55.
[5] M. Kamperman, E. Kroner, A. Del Campo, R. M. McMeeking, E. Arzt, *Adv. Eng. Mater.* **2010**, *12*, 335.
[6] M. Sitti, R. S. Fearing, *J. Adhes. Sci. Technol.* **2003**, *17*, 1055.
[7] A. Ghatak, L. Mahadevan, J. Y. Chung, M. K. Chaudhury, V. Shenoy, *Proc. R. Soc. A* **2004**, *460*, 2725.
[8] Y. Tian, N. Pesika, H. Zeng, K. Rosenberg, B. Zhao, P. McGuiggan, K. Autumn, J. Israelachvili, *Proc. Natl. Acad. Sci. U. S. A.* **2006**, *103*, 19320.
[9] M. P. Murphy, B. Aksak, M. Sitti, *Small* **2009**, *5*, 170.
[10] Y. Mengüç, S. Y. Yang, S. Kim, J. A. Rogers, M. Sitti, *Adv. Funct. Mater.* **2012**, *22*, 1246.
[11] S. Kim, E. Cheung, M. Sitti, *Langmuir* **2009**, *25*, 7196.
[12] Y. Mengüç, M. Röhrig, U. Abusomwan, H. Hölscher, M. Sitti, *J. R. Soc., Interface* **2014**, *11*, 20131205.
[13] X. Li, D. Tao, H. Lu, P. Bai, Z. Liu, L. Ma, Y. Meng, Y. Tian, *Surf. Topogr.: Metrol. Prop.* **2019**, *7*, 023001.
[14] C. Greiner, E. Arzt, A. Del Campo, *Adv. Mater.* **2009**, *21*, 479.
[15] M. P. Murphy, S. Kim, M. Sitti, *ACS Appl. Mater. Interfaces* **2009**, *1*, 849.
[16] H. K. Minsky, K. T. Turner, *Appl. Phys. Lett.* **2015**, *106*, 201604.
[17] S. C. L. Fischer, E. Arzt, R. Hensel, *ACS Appl. Mater. Interfaces* **2017**, *9*, 1036.
[18] D. M. Drotlef, C. B. Dayan, M. Sitti, *Integr. Comp. Biol.* **2019**, *59*, 227.
[19] V. Liimatainen, D. M. Drotlef, D. Son, M. Sitti, *Adv. Mater.* **2020**, *32*, 2000497.


© 2021 The Authors. Small published by Wiley-VCH GmbH

[20] M. K. Kwak, H. E. Jeong, K. Y. Suh, *Adv. Mater.* **2011**, *23*, 3949.
[21] W. G. Bae, D. Kim, M. K. Kwak, L. Ha, S. M. Kang, K. Y. Suh, *Adv. Healthcare Mater.* **2013**, *2*, 109.
[22] D. M. Drotlef, M. Amjadi, M. Yunusa, M. Sitti, *Adv. Mater.* **2017**, *29*, 1701353.
[23] S. Song, M. Sitti, *Adv. Mater.* **2014**, *26*, 4901.
[24] S. Song, D.-M. Drotlef, C. Majidi, M. Sitti, *Proc. Natl. Acad. Sci. U. S. A.* **2017**, *114*, E4344.
[25] B. Aksak, M. P. Murphy, M. Sitti, *2008 IEEE Int. Conf. on Robotics and Automation*, IEEE, Piscataway, NJ **2008**, pp. 3058–3063.
[26] S. Kim, M. Spenko, S. Trujillo, B. Heyneman, D. Santos, M. R. Cutkosky, *IEEE Trans. Rob.* **2008**, *24*, 808.
[27] M. P. Murphy, C. Kute, Y. Mengüç, M. Sitti, *Int. J. Rob. Res.* **2011**, *30*, 118.
[28] H. Gao, H. Yao, *Proc. Natl. Acad. Sci. U. S. A.* **2004**, *101*, 7851.
[29] A. Del Campo, C. Greiner, E. Arzt, *Langmuir* **2007**, *23*, 10235.
[30] C. Greiner, A. Del Campo, E. Arzt, *Langmuir* **2007**, *23*, 3495.
[31] A. V. Spuskanyuk, R. M. McMeeking, V. S. Deshpande, E. Arzt, *Acta Biomater.* **2008**, *4*, 1669.
[32] N. A. Fleck, S. N. Khaderi, R. M. McMeeking, E. Arzt, *J. Mech. Phys. Solids* **2017**, *101*, 30.
[33] B. Aksak, K. Sahin, M. Sitti, *Beilstein J. Nanotechnol.* **2014**, *5*, 630.
[34] B. Aksak, C.-Y. Y. Hui, M. Sitti, *J. R. Soc., Interface* **2011**, *8*, 1166.
[35] L. Heepe, A. E. Kovalev, A. E. Filippov, S. N. Gorb, *Phys. Rev. Lett.* **2013**, *111*, 104301.
[36] L. Heepe, S. N. Gorb, *Annu. Rev. Mater. Res.* **2014**, *44*, 173.
[37] M. Varenberg, S. Gorb, *J. R. Soc., Interface* **2008**, *5*, 785.
[38] S. Gorb, M. Varenberg, A. Peressadko, J. Tuma, *J. R. Soc., Interface* **2007**, *4*, 271.
[39] S. Kim, M. Sitti, *Appl. Phys. Lett.* **2006**, *89*, 261911.
[40] M. P. Murphy, B. Aksak, M. Sitti, *J. Adhes. Sci. Technol.* **2007**, *21*, 1281.
[41] G. Carbone, E. Pierro, *Small* **2012**, *8*, 1449.
[42] R. G. Balijepalli, M. R. Begley, N. A. Fleck, R. M. McMeeking, E. Arzt, *Int. J. Solids Struct.* **2016**, *85*, 160.
[43] G. Carbone, E. Pierro, S. N. Gorb, *Soft Matter* **2011**, *7*, 5545.
[44] G. S. Hornby, A. Globus, D. S. Linden, J. D. Lohn, *Automated Antenna Design with Evolutionary Algorithms*, American Institute of Aeronautics and Astronautics, Reston, VA **2006**, p. 7242.
[45] C. Bisagni, L. Lanzi, *Compos. Struct.* **2002**, *58*, 237.
[46] G. X. Gu, C. T. Chen, M. J. Buehler, *Extreme Mech. Lett.* **2018**, *18*, 19.
[47] C. H. Yu, Z. Qin, M. J. Buehler, *Nano Futures* **2019**, *3*, 035001.
[48] C. M. Hamel, D. J. Roach, K. N. Long, F. Demoly, M. L. Dunn, H. J. Qi, *Smart Mater. Struct.* **2019**, *28*, 065005.
[49] I. Santos, J. Nieves, Y. K. Penya, P. G. Bringas, in *2009 Iccas-Sice*, IEEE, Piscataway, NJ **2009**, pp. 4536–4541.
[50] G. Pilania, C. Wang, X. Jiang, S. Rajasekaran, R. Ramprasad, *Sci. Rep.* **2013**, *3*, 2810.
[51] A. Mannodi-Kanakkithodi, G. Pilania, T. D. Huan, T. Lookman, R. Ramprasad, *Sci. Rep.* **2016**, *6*, 20952.
[52] O. Hennigh, in *6th Int. Conf. Learn Represent ICLR 2018 - Work. Track Proc*, **2018**, pp. 1–12.
[53] M. Shimoda, T. Nagano, J. X. Shi, *Struct. Multidiscip. Optim.* **2019**, *59*, 1543.
[54] C. Chen, Y. Zuo, W. Ye, X. Li, Z. Deng, S. P. Ong, *Adv. Energy Mater.* **2020**, *10*, 1903242.
[55] J. Snoek, H. Larochelle, R. P. Adams, *Advances in Neural Information Processing Systems*, (Eds: F. Pereira, C. J. C. Burges, L. Bottou, K. Q. Weinberger), Curran Associates, Inc., New York **2012**, pp. 2960–2968.
[56] B. Shahriari, K. Swersky, Z. Wang, R. P. Adams, N. De Freitas, *Proc. IEEE* **2015**, *104*, 148.
[57] E. Brochu, V. M. Cora, N. De Freitas, arXiv1012.2599 **2010**.
[58] H. J. Kushner, *J. Basic Eng.* **1964**, *86*, 97.
[59] M. A. Osborne, R. Garnett, S. J. Roberts, in *3rd International Conference on Learning and Intelligent Optimization (LION3)*, **2009**, pp. 1–15.
[60] D. R. Jones, *J. Global Optim.* **2001**, *21*, 345.
[61] Y. Kim, C. Yang, Y. Kim, G. X. Gu, S. Ryu, *ACS Appl. Mater. Interfaces* **2020**, *12*, 24458.
[62] M. E. Mortenson, *Mathematics for Computer Graphics Applications*, Industrial Press Inc., New York **1999**.
[63] D. M. Hawkins, *J. Chem. Inf. Comput. Sci.* **2004**, *44*, 1.
[64] M. Mooney, *J. Appl. Phys.* **1940**, *11*, 582.
[65] R. S. Rivlin, *Philos. Trans. R. Soc., A* **1948**, *241*, 379.
[66] D. S. Dugdale, *J. Mech. Phys. Solids* **1960**, *8*, 100.
[67] G. I. Barenblatt, *Adv. Appl. Mech.* **1962**, *7*, 55.
[68] T. Tang, C. Y. Hui, N. J. Glassmaker, *J. R. Soc., Interface* **2005**, *2*, 505.
[69] R. Calandra, A. Seyfarth, J. Peters, M. P. Deisenroth, *Ann. Math. Artif. Intell.* **2016**, *76*, 5.
[70] D. Sameoto, C. Menon, *Smart Mater. Struct.* **2010**, *19*, 103001.
[71] V. Kanyanta, A. Ivankovic, *J. Mech. Behav. Biomed. Mater.* **2010**, *3*, 51.
[72] S. N. Khaderi, N. A. Fleck, E. Arzt, R. M. McMeeking, *J. Mech. Phys. Solids* **2015**, *75*, 159.
[73] M. Micciché, E. Arzt, E. Kroner, *ACS Appl. Mater. Interfaces* **2014**, *6*, 7076.
[74] I. D. Johnston, D. K. McCluskey, C. K. L. Tan, M. C. Tracey, *J. Micromech. Microeng.* **2014**, *24*, 035017.
[75] D. Maugis, *Contact, Adhesion and Rupture of Elastic Solids*, Springer Science & Business Media, Berlin **2013**.
[76] L. F. Boesel, C. Cremer, E. Arzt, A. Del Campo, *Adv. Mater.* **2010**, *22*, 2125.
[77] R. Hensel, K. Moh, E. Arzt, *Adv. Funct. Mater.* **2018**, *28*, 1800865.
[78] G. M. Guidoni, D. Schillo, U. Hangen, G. Castellanos, E. Arzt, R. M. McMeeking, R. Bennewitz, *J. Mech. Phys. Solids* **2010**, *58*, 1571.
[79] H. Marvi, S. Song, M. Sitti, *Langmuir* **2015**, *31*, 10119.
[80] R. G. Balijepalli, M. R. Begley, N. A. Fleck, R. M. McMeeking, E. Arzt, *Int. J. Solids Struct.* **2016**, *160*, 85.
[81] A. Filippov, V. L. Popov, S. N. Gorb, *J. Theor. Biol.* **2011**, *276*, 126.
[82] B. S. Bschaden, *M.Sc. Thesis*, University of Alberta, **2014**.
[83] D. Sameoto, in *Bio-Inspired Structured Adhesives*, Vol. *9*, Springer, Cham **2017**, pp. 221–244.


© 2021 The Authors. Small published by Wiley-VCH GmbH